THE ASTROPHYSICAL JOURNAL, 465:825–839, 1996 July 10

A SEARCH FOR STAR FORMATION IN THE TRANSLUCENT CLOUD MBM 40

LORIS MAGNANI, JEAN-PIERRE CAILLAULT, AND THOMAS HEARTY
Department of Physics and Astronomy, University of Georgia, Athens, GA 30602-2451
JOHN STAUFFER
Harvard/Smithsonian Center for Astrophysics, Cambridge, MA 02138
J. H. M. M. SCHMITT AND RALPH NEUHÄUSER
Max-Planck-Institut für Extraterrestrische Physik, 85740 Garching, Germany
AND
FRANCES VERTER AND ELI DWEK
NASA/Goddard Space Flight Center, Greenbelt, MD 20771
Received 1995 July 17; accepted 1996 February 12

ABSTRACT

The star formation status of the translucent high-latitude molecular cloud, MBM 40, is explored through analysis of radio, infrared, optical, and X-ray data. With a peak visual extinction of 1 to 2 mag, MBM 40 is an example of a high-latitude cloud near the diffuse/translucent demarcation. However, unlike most translucent clouds, MBM 40 exhibits a compact morphology and a kinetic energy–to–gravitational potential energy ratio near unity. Our radio data, encompassing the CO ($J = 1$–0), CS ($J = 2$–1), and H_2CO 1_{11}–1_{10} spectral line transitions, reveal that the cloud contains a ridge of molecular gas with $n \geq 10^3$ cm^{-3}. In addition, the molecular data, together with *IRAS* data, indicate that the mass of MBM 40 is $\sim 40\ M_\odot$. In light of the ever-increasing number of recently formed stars far from any dense molecular clouds or cores, we searched the environs of MBM 40 for any trace of recent star formation.

We used the *ROSAT* All-Sky Survey X-ray data and a *ROSAT* PSPC pointed observation toward MBM 40 to identify 33 stellar candidates with properties consistent with pre–main-sequence (PMS) stars. Follow-up optical spectroscopy of the candidates with $V < 15.5$ was conducted with the 1.5 m Fred Lawrence Whipple Observatory telescope in order to identify signatures of T Tauri or pre–main-sequence stars (such as the Li 6708 Å resonance line).

Since none of our optically observed candidates display standard PMS signatures, we conclude that MBM 40 displays no evidence of recent or ongoing star formation. The absence of high-density molecular cores in the cloud and the relatively low column density compared to star-forming interstellar clouds may be the principal reasons that MBM 40 is devoid of star formation. More detailed comparison between this cloud and other, higher extinction translucent and dark clouds may elucidate the necessary initial conditions for the onset of low-mass star formation.

Subject headings: ISM: clouds — ISM: individual (MBM 40) — ISM: molecules — radio lines: ISM — stars: formation — stars: pre–main-sequence — X-rays: stars

1. INTRODUCTION

MBM 40 is a small (0.7 deg^2), isolated low-extinction cloud located at $l = 37\overset{\circ}{.}6$ and $b = 44\overset{\circ}{.}7$ projected on the North Polar Spur. The cloud was first listed (and misidentified) as an H II nebulosity by Sharpless (1959) who included the nebula as object 73 in his catalog. Lynds (1965) identified two bright nebulae (LBN 105 and 106) in the immediate vicinity of the cloud, and both Verschuur (1974) and Colomb, Pöppel, & Heiles (1980) readily identified a narrow H I feature at $v_{LSR} = 4$ km s^{-1} at this location. Molecular gas was first detected in the cloud by Blitz, Fich, & Stark (1982) during their survey of CO ($J = 1$–0) emission from the Sharpless objects. The CO detection was along a single line of sight, and no mapping of the region was made. It was not until the cloud was included as object 40 of the Magnani, Blitz, & Mundy (1985, hereafter MBM) high-latitude CO survey that its spatial extent and mass were determined. A poorly sampled map of the cloud (10′ sampling with a 2.3 beam) in the CO ($J = 1$–0) line is shown by MBM. A fully sampled map of the same object (referred to as the Hercules cloud) was also accomplished by de Vries (1988) in the CO ($J = 1$–0) transition with a beam resolution of 8.7; the de Vries map of the cloud closely resembles the MBM version.

The distance to this cloud is established by Welty et al. (1989) as ≤ 140 pc from echelle spectroscopy of the Na I absorption line and is fully consistent with the statistical estimate of the distance to the high-latitude clouds in general (~ 100 pc; MBM). Penprase (1993) has improved the distance estimate to $90 < d < 150$ pc with additional observations of foreground stars. We adopt 100 pc as the distance to the cloud in the remainder of this paper.

MBM 40 is a typical example of a low-extinction translucent cloud. These objects are easily identifiable at high Galactic latitudes away from the background confusion of the plane and represent the molecular component of the *IRAS* cirrus (Weiland et al. 1986). Translucent clouds span a vast range of sizes, shapes, and masses, but they can be broadly categorized into two basic morphological types: compact and filamentary. MBM 40 is typical of the former type of high-latitude translucent cloud. It differs significantly from morphologically similar *dark* clouds in that its visual extinction is nowhere greater than 2 mag. In this

paper the overall structure of MBM 40 is revealed from extensive observations of several molecular species (CO, CS, and H_2CO) and from *IRAS* 100 μm data.

As a class of object, the translucent clouds present some compelling questions for the study of small molecular clouds and the diffuse interstellar medium. Translucent molecular clouds are an intermediate population situated between diffuse and dark clouds as regards H_2 column density [$\equiv N(H_2)$], visual extinction, and astrochemical complexity. Van Dishoeck & Black (1988) define dark clouds as those entities with at least some region at $A_V \geq 5$ mag and diffuse clouds as objects in which the extinction is nowhere greater than 1 mag. MBM 40 is thus near the transition between diffuse and translucent clouds. Dark clouds and Bok globules are known sites of low-mass star formation (see, e.g., Myers & Benson 1983; Yun & Clemens 1990), while traditional diffuse molecular clouds (e.g., the cloud along the line of sight to ζ Ophiuchi) cannot form stars (Elmegreen 1993). The principal reason for this inability to form stars is believed to be the dearth of high-density, bound cores in the diffuse clouds.

In contrast, the star-forming capability of translucent clouds is still unknown. High-density regions somewhat similar to those found in dark clouds have been found in several translucent clouds (Turner, Xu, & Rickard 1992; Mebold, Heithausen, & Reif 1987; Meyerdierks, Brouillet, & Mebold 1990; Schreieber et al. 1993; and Reach et al. 1995). If dense cores are present in the translucent molecular clouds, then low-mass star formation is possible in these objects, and any inventory of the local star formation rate must include the nonnegligible number of translucent clouds in the local interstellar medium (Magnani 1994). However, even in the absence of high-density cores, some scenarios have been developed for the creation of low-mass stars in relatively low-density environments (§ 2).

Previous attempts to determine whether star formation is possible in translucent clouds include searches through infrared databases (the *IRAS* Point Source Catalog—Magnani, Caillault, & Armus 1990; the IRAS Faint Source Survey—Magnani et al. 1995) and the *Einstein* X-ray database (Caillault, Magnani, & Fryer 1995). Although the first two investigations produced many candidates that still require optical spectroscopy for ultimate confirmation, no unambiguous pre–main-sequence (PMS) or T Tauri star has been found in a *low-extinction* translucent cloud to date. We note that MBM 12 contains T Tauri stars (Magnani et al. 1995; Pound 1996), but, with a central extinction of 4–5 mag, this object resembles more closely a dark rather than a translucent cloud. Our first three papers on star formation in translucent clouds focused on global surveys; in this paper, we examine in detail a single translucent cloud. Molecular, infrared, optical, and X-ray data for MBM 40 are analyzed in order to determine whether this particular cloud has formed or is in the process of forming low-mass stars, but we do this primarily by identifying X-ray point sources within or near the cloud.

Observations of known star-forming regions have revealed large numbers of X-ray–emitting sources (see, e.g., Feigelson et al. 1987 and Neuhäuser et al. 1995b), most of which had not been previously known to be PMS stars (Walter et al. 1988; Alcalá et al. 1995; Neuhäuser et al 1995c; Wichmann et al. 1995). However, X-ray emission by itself is not a sufficient condition for positively identifying a PMS star; follow-up spectroscopic observations of the optical counterparts to the X-ray sources are needed to determine their pedigree unambiguously. The standard signature for such youthful stars is Li 6708 Å absorption. This is seen in both classical T Tauri stars (CTTS; those with strong Hα emission) and weak T Tauri stars (WTTS; those with weak or absent Hα emission). Other useful spectroscopic diagnostics would be radial velocities, rotational velocities, or the width and profile of the Hα and Ca emission lines (if present)—however, these diagnostics require high-dispersion spectra. Using the 1.5 m Fred Lawrence Whipple Observatory telescope, we obtained moderate-dispersion spectra of candidate sources in order to determine readily whether the Li 6708 Å absorption line was present in any of them.

In the following sections we describe our data acquisition and reduction analyses, the rationale for searching for youthful stars in this particular cloud, our results, and their implications.

2. THE STRUCTURE OF THE CLOUD FROM MOLECULAR AND INFRARED DATA

For star formation to occur in a molecular cloud, it is generally considered necessary that the cloud contain dense molecular concentrations typically known as "cores." These objects are the precursors of low-mass stars and are often identified by probing the cloud with high-density tracers such as NH_3 and CS. Myers (1985) defines low-mass cores to be regions of size $\sim$0.05–0.2 pc, log $n \sim 4$–5, $T \sim 9$–12 K, and $\Delta v \sim 0.2$–0.4 km s^{-1}. Since these types of cores give rise to T Tauri stars in dark molecular clouds, their existence in MBM 40 would constitute circumstantial evidence that the cloud could be forming stars. However, recent evidence from observations of high-latitude B stars in the halo indicates that some of these objects are not runaway stars from the Galactic plane and, thus, must have formed in situ (Keenan et al. 1986; Conlon 1993). In addition, the recent discovery of 11 T Tauri stars more than 10° south of the Taurus-Auriga dark clouds (Neuhäuser et al. 1995b) and earlier reports of T Tauri stars far from any known molecular cloud or core (Rucinski & Krauttner 1983; Downes & Keyes 1988; de la Reza et al 1989; Gregorio-Hetem et al. 1992) may indicate that star formation is possible in regions with densities lower than previously thought. In light of these results, the possibility of stars forming in regions with no traces of the "standard" dark cloud cores cannot be excluded a priori. Some theoretical work attempts to explain the formation of stars in low-density gas as a result of gravitational collapse induced by either cloudlet-cloudlet collisions (Dyson & Hartquist 1983), the merger of a gas-rich satellite galaxy with our own (Rodgers, Harding, & Sadler 1981; Lance 1988), the impact of high-velocity clouds onto the Galactic disk (Lépine & Duvert 1994), or a phase transition (Christodoulou & Tohline 1990). This recent trend makes the question of star formation in translucent clouds more relevant since, in general, these objects either do not contain any dense molecular cores or, at most, a few.

From a more global perspective, most of the translucent high-latitude clouds are known to be gravitationally unbound (MBM). In other words, the gravitational potential energy of the clouds is typically 1–2 orders of magnitude less than the kinetic energy as derived from the clump-to-clump velocity dispersion. Although there is some evidence that a fraction of the clouds may be confined by the pressure

of the external medium (see, e.g., Keto & Myers 1986), some of the clouds would require external pressures, P/k, of order 10^5 cm^{-3} K for confinement, much higher than any currently accepted value for the ISM. If these clouds are not bound, they are then transient objects with lifetimes on the order of the sound-crossing time (10^6 yr). It is difficult to envision star formation in unbound objects of this type with such short dynamical lifetimes (Elmegreen 1993). However, the ratio of the kinetic to gravitational potential energy in MBM 40 is close to unity (MBM). Incorporating new mass estimates from our molecular and infrared data allows us to determine more accurately the global dynamic state of the cloud; we elaborate on these topics below.

2.1. *Are Low-Mass Cores Present in MBM 40?*

2.1.1. CO *and* H_2CO *Considerations*

The ^{12}CO ($J = 1$–0) and ^{13}CO ($J = 1$–0) data for MBM 40 were obtained in 1984 from the now-defunct 5 m telescope of the Millimeter-Wave Observatory[1] (MWO) near Fort Davis, Texas and with the NRAO[2] 12 m telescope at Kitt Peak during 1985 May. The observing procedure and parameters are described by MBM for the MWO run and by Magnani, Blitz, & Wouterloot (1988) for the NRAO run. The Gaussian-fit parameters for the individual spectra are included in the latter paper in their Tables 3 and 4. We note that in Table 3 of Magnani et al. (1988) the v_{LSR} velocities are too large by 0.49 km s^{-1}. This error in the velocity scale (corresponding to a shift of three channels) was produced by an internal software error at MWO during the fall of 1984.

The H_2CO observations were carried out at the NRAO 43 m telescope in Green Bank, West Virginia on 1990 May 18–31. The front end consisted of a cooled, single-beam, corrugated, dual-hybrid mode feed sensitive to both circular polarizations. The autocorrelator was configured into two subcorrelators of 512 channels each with 0.625 MHz bandwidth. The data were obtained in the frequency-switched mode with the frequency throw plus and minus one-quarter of the bandpass so that the H_2CO 1_{11}–1_{10} transition appeared in both the signal and reference bandpasses. The two polarizations were averaged together, and the resulting spectrum was folded so that the effective velocity coverage was 19 km s^{-1} and the velocity resolution was 0.08 km s^{-1}. Typical system temperatures in clear weather at elevations greater than 40° were 27–30 K for the two channels. The spectra were calibrated with noise tubes the values of which were provided by the Green Bank engineering staff. To convert the observed antenna temperature to brightness temperature, T_B, we use a beam efficiency of 0.67 (R. Maddalena, private communication). The system stability was monitored by observing TMC-1 throughout the run. The antenna temperature at the central position of that cloud, $(\alpha:\delta) = (04^h38^m38^s:25°35'45'')$, was -0.50 K with a variation of less than 5% over the course of the observing run.

A square 8×8 grid was mapped at full beamwidth resolution (i.e., in 6′ steps) with typical integration times of 30–40 minutes per point. The resulting rms noise level was 10–15 mK after Hann smoothing. If the presence of a line was suspected, a deeper integration was carried out. All of our detected lines are listed in Table 1 along with the Gaussian-fit parameters that were obtained from the unsmoothed data.

The CO ($J = 1$–0) map of MBM 40 presented in MBM is still the only published full-scale CO map of this region. Although undersampled, the map reveals the general structure of the cloud: a somewhat spheroidal region with a southeast to northwest ridge or spine extending diagonally through the cloud. A smaller ridge is present to the northeast of and parallel to the main ridge and is prominent both on the H_2CO and infrared maps (see below). The two parallel ridges are also noticeable as regions of diffuse optical emission on the Palomar Observatory Sky Survey (POSS) prints and were misidentified by Sharpless (1959) as a low-intensity level H II region. The optical emission is partly due to the dust in the cloud reflecting the integrated starlight from the Galactic plane and is a common feature of the high-latitude clouds (Sandage 1976; Jura 1979). Recent work by Guhathakurta & Cutri (1994) invokes luminescence of small hydrogenated carbon grains as the primary cause of the red optical reflection.

Better sampled CO data are presented in Figures 1*a* and 1*b* for the lower section of the main ridge. The MWO data are sampled at 2.′5 spacing with a 2.′3 beam at 115 GHz. The numbers associated with some of the observed positions give the ratio of the ^{12}CO to ^{13}CO integrated antenna temperature [$\equiv W(^{12}CO)/W(^{13}CO)$] for that particular line of sight. In Figure 1*b*, the numbers within the circled regions are the $W(^{12}CO)/W(^{13}CO)$ ratios based on higher resolution (1′) data from the NRAO 12 m telescope. Table 2 lists the $W(^{12}CO)/W(^{13}CO)$ ratio, the ^{13}CO optical depth as calculated under LTE assumptions (Dickman 1978—we assume $T_{ex} = 10$ K), the ^{13}CO column density, the H_2 column density based on an assumed constant $^{13}CO/H_2$ abundance of 2.5×10^{-6}, and the $N(H_2)/W(CO)$ ratio (defined as X_{CO} or the "X" factor) determined from the tabulated $N(H_2)$ value and ^{12}CO data for the same line of sight reported in Magnani et al. (1988).

With the estimate of $N(H_2)$ in Table 2 and the assump-

TABLE 1

H_2CO 1_{11}–1_{10} LINE PARAMETERS FOR MBM 40

R.A. (1950)	Decl. (1950)	$-T_A$ (mK)	Δv (km s^{-1})	v_{LSR} (km s^{-1})
16^{h}07^{m}36^s.....	22°04′00″	23 ± 2	1.00 ± 0.13	3.07 ± 0.05
16 07 36	22 10 00	46 ± 4	0.84 ± 0.34	2.69 ± 0.07
16 08 00	22 04 00	61 ± 9	0.84 ± 0.15	2.92 ± 0.06
16 08 00	22 10 00	82 ± 8	0.92 ± 0.10	2.80 ± 0.04
16 08 00	22 16 00	37 ± 7	1.21 ± 0.27	2.70 ± 0.11
16 08 24	21 52 00	48 ± 8	0.76 ± 0.16	3.22 ± 0.07
		40 ± 11[a]	0.44 ± 0.16	
16 08 24	21 58 00	57 ± 6	0.78 ± 0.11	3.12 ± 0.04
16 08 24	22 04 00	46 ± 11	0.43 ± 0.12	3.06 ± 0.05
16 08 24	22 10 00	36 ± 10	0.68 ± 0.22	2.59 ± 0.09
16 08 24	22 16 00	37 ± 6	0.53 ± 0.09	2.85 ± 0.04
16 08 48	21 46 00	26 ± 8	0.94 ± 0.34	3.12 ± 0.15
16 08 48	21 52 00	101 ± 16	0.59 ± 0.11	3.21 ± 0.05
16 08 48	21 58 00	57 ± 14	0.48 ± 0.14	3.18 ± 0.06
16 08 48	22 10 00	62 ± 10	0.68 ± 0.13	2.87 ± 0.06
16 09 12	21 46 00	32 ± 4	1.15 ± 0.19	3.12 ± 0.08
16 09 12	21 46 00	79 ± 11	0.23 ± 0.04	3.35 ± 0.02
		66 ± 18[a]	0.17 ± 0.05	
16 09 36	22 04 00	20 ± 3	0.68 ± 0.14	3.03 ± 0.06
		11 ± 3[a]	0.70 ± 0.27	

[a] $F = 0$–1 hyperfine component of the H_2CO 1_{11}–1_{10} transition.

[1] The Millimeter Wave Observatory was operated by the Electrical Engineering Research Laboratory of the University of Texas at Austin with support from the National Science Foundation and McDonald Observatory.

[2] The National Radio Astronomy Observatory is operated by Associated Universities, Inc., under contract with the National Science Foundation.

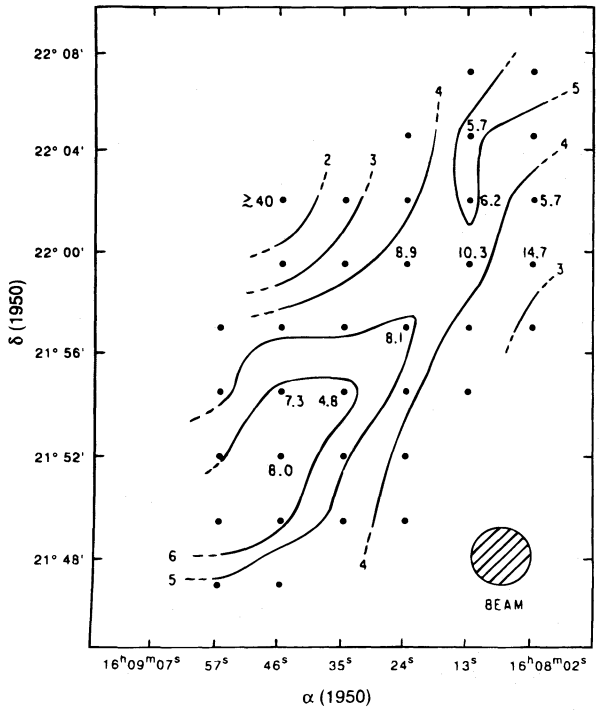

FIG. 1a

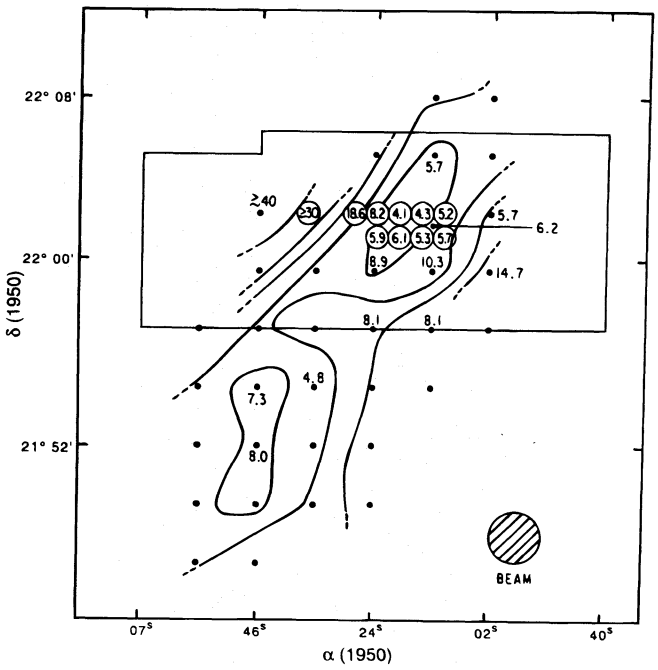

FIG. 1b

FIG. 1.—(*a*) Integrated CO ($J = 1$–0) antenna temperature map of the central region of MBM 40 main ridge described in the text. The contours are set at 2, 3, 4, etc. K km s^{-1}, and the value of each particular contour is indicated at one of the endpoints. The black dots represent the sampled positions with the 2.3 beam, and the two-digit numerals sometimes associated with the black dots are the ratio of the integrated $^{12}CO/^{13}CO$ antenna temperatures for that particular line of sight. The absence of a $^{12}CO/^{13}CO$ ratio next to a dot indicates that ^{13}CO data were not available for that position. (*b*) Same as (*a*), except that the contours represent the CO ($J = 1$–0) antenna temperature, T_A^*. The contour levels begin at 3.5 K, and each succeeding level is 1 K greater than the previous level. The nearly rectangular box centered on the upper clump represents the boundary of the area mapped at 1′ resolution with the NRAO 12 m telescope (see Fig. 2). The circles represent the lines of sight for which ^{13}CO ($J = 1$–0) data from the 12 m telescope are available, and the number within the circles is the ratio of the integrated $^{12}CO/^{13}CO$ antenna temperatures.

TABLE 2

COLUMN DENSITIES

R.A. (1950)	Decl. (1950)	$^{12}CO/^{13}CO$	$\tau(^{13}CO)$	$N(^{13}CO) \times 10^{14}$ (cm^{-2})	$N(H_2) \times 10^{20}$ (cm^{-2})	$X_{CO} \times 10^{20}$ (cm^{-2} [K km s^{-1}]$^{-1}$)
Column Densities from ^{13}CO–MWO Data						
16h08m02s.....	21°59′.5	14.7	0.05	1.9	0.8	0.3
16 08 02	22 02.0	5.7	0.22	6.9	2.8	0.9
16 08 13	22 02.0	6.2	0.35	10.1	4.0	0.8
16 08 13	22 04.5	5.7	0.43	10.8	4.3	0.9
16 08 14	21 59.5	10.3[a]	0.20	5.3	2.1	0.7
16 08 24	21 57.0	8.1	0.13	6.9	2.8	0.4
16 08 24	21 59.5	8.9	0.20	5.9	2.4	0.5
16 08 35	21 54.5	4.8	0.60	18.0	7.2	1.1
16 08 46	21 52.0	8.0	0.33	10.3	4.1	0.6
16 08 46	21 54.5	7.3	0.33	10.3	4.1	0.7
Column Densities from ^{13}CO–NRAO Data						
16 08 11	22 01.0	5.7	0.44	7.8	3.1	0.7
16 08 11	22 02.0	5.2	0.74	13.1	5.2	1.1
16 08 15	22 01.0	5.3	0.59	13.9	5.6	0.9
16 08 15	22 02.0	4.3	0.64	15.1	6.0	1.2
16 08 19	22 01.0	6.1	0.42	7.4	3.0	0.6
16 08 19	22 02.0	4.1	0.40	11.8	4.7	1.1
16 08 24	22 01.0	5.9	0.37	8.7	3.5	0.8
16 08 24	22 02.0	8.2	0.25	4.4	1.8	0.4
16 08 28	22 02.0	18.6	0.08	1.9	0.8	0.2

[a] Includes two ^{12}CO components and one ^{13}CO component; τ and the other parameters are calculated for only the single component.

tion that the two clumps in the ridge are as thick as they are wide, densities of several times 10^3 cm^{-3} are derived for the condensations along the ridge. Since $W(^{12}CO)/W(^{13}CO)$ ratios in the range 4–8 are indicative of optically thick ^{12}CO emission, it follows from the data presented in Figure 1 that the ridge stands out significantly with respect to the surrounding gas of the cloud, which has an average density of order 10^2 cm^{-3} (MBM). The central and southern portions of the ridge, in which the optical depth of the ^{12}CO is greatest, appear to consist of two clumps (immediately recognizable in Fig. 1*b*) that are denser than the surrounding gas. The linear size of these clumps is $\sim 5'$, corresponding to 0.15 pc at the adopted distance of MBM 40.

Although the LTE method works best in clouds with $5 < A_V < 10$ mag (Dickman 1978), the values of $N(H_2)$ we obtain with this technique are consistent with those obtained for lines of sight in MBM 40 where we have CH data (Magnani et al. 1996b). It is unlikely that our estimate of the column density of the molecular ridge is off by more than a factor of a few. In any case, a greater source of uncertainty in determining the volume density is the estimate of the pathlength through the cloud. This estimate is usually based on the linear dimensions of structures across the face of the cloud, and the extrapolation to the radial direction is often hazardous.

At lower resolution (6′), the H_2CO observations of the clouds are shown in Figure 2. The main ridge visible in CO is clearly present, as is the other ridge to the northeast. Since the H_2CO absorption covers a smaller area than the CO emission (0.2 deg^2 vs. 0.7 deg^2), and the average H_2CO line width is narrower than the average CO line width (0.75 km s^{-1} vs. 0.80 km s^{-1}), it is reasonable to assume that the H_2CO is tracing slightly denser gas than the CO. Thus, Figure 2 shows the presence of two well-defined condensations that are similar in size to the low-mass cores

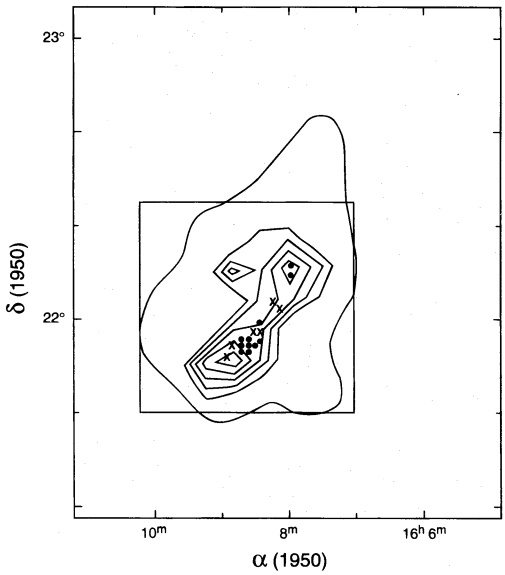

FIG. 2.—Map of MBM 40 in the H_2CO 1_{10}–1_{11} transition. The bold, outer contours of the map illustrate the extent of the CO ($J = 1$–0) transition as mapped by MBM. The square box represents the region sampled in H_2CO, and the contours of the 6 cm absorption line are within the box. The outermost contour (signifying the lowest level of absorption) is at −20 mK, and each succeeding contour is at an interval of 20 mK. Within the H_2CO contours are the locations of the lines of sight sampled in the CS ($J = 2$–1) transition. Detections are denoted by filled circles, and nondetections are denoted by crosses. The Gaussian fit parameters and rms limits for nondetections are listed in Tables 1 and 3.

described by Myers (1985). However, a comparison between the H_2CO map and the CO map in Figure 1*b* reveals a surprising feature: The northwest clump in the CO map of Figure 1*b* is actually located within a region of relatively weak H_2CO absorption. We may be able to understand this anticorrelation in light of the excitation characteristics of the 6 cm transition of H_2CO.

The excitation of the H_2CO 1_{11}–1_{10} (6 cm) and 2_{12}–2_{11} (2 cm) transitions is anomalous in the sense that for molecular cloud densities less than 10^6 cm^{-3}, the lines appear in absorption against the cosmic microwave background radiation. The excess population in the lower levels of the pertinent $J = 1$, 2 states requires a nonthermal mechanism first suggested by Townes & Cheung (1969). The refrigeration pump for the 6 cm and 2 cm transitions is initiated by collisions with H_2 preferentially populating the lower level of the 2 cm doublet (2_{12}) state. This is rapidly followed by radiative decay to the lower level of the 6 cm doublet (1_{11}) state, so that both doublets have greater than equilibrium populations in their lower levels. The net result is that the excitation temperature for both transitions is below the microwave background temperature. However, at high enough densities (typically $\geq 10^6$ cm^{-3} for the 6 cm line and somewhat less for the 2 cm line), the collisions with H_2 are sufficient in number to begin thermalizing the level populations so that lines appear in emission rather than absorption. The behavior of the excitation temperature of the 6 and 2 cm transitions of H_2CO as a function of density is described by Evans et al. (1975).

A weak H_2CO 6 cm absorption feature may thus indicate either the presence of very low density molecular gas or of much higher density gas as the transition passes from absorption to emission. In these latter instances, there will be an anticorrelation between the integrated H_2CO antenna temperature and that of CO. This anticorrelation has already been noted in a translucent high-latitude cloud by Heithausen, Mebold, & de Vries (1987) even though later work by the same group reversed this claim (Meyerdierks et al. 1990).

In MBM 40, we note that the H_2CO and CO line strengths are for the most part correlated along the ridge region, but there exists a clear anticorrelation at $(\alpha:\delta) = (16^h08^m20^s:22°02'00'')$. The $W(^{12}CO)/W(^{13}CO)$ ratio is as low as 4–5 in this region (see Fig. 1*b*), indicative of optically thick gas, yet the H_2CO 6 cm absorption is only at the ~ 40 mK level, significantly lower than in the southern and northern sections of the ridge. In light of the above argument, it is plausible that a low-mass core may be present even at this location. We do note that H_2CO has a relatively large dipole moment so that it may be possible for electron excitation to lower the gas densities necessary for the transition to pass from absorption to emission (see, e.g., Turner 1993). Future studies with higher density gas tracers such as NH_3 or the CS ($J = 5$–4) transition are required to settle this matter.

In summary, our CO and H_2CO observations indicate that densities of at least 10^3 cm^{-3} are present along the molecular ridge in MBM 40. Whether higher density regions reminiscent of those found in dark cloud "cores" are present cannot be determined from these data.

2.1.2. CS ($J = 2$–1) *Observations along the Ridge*

The CS ($J = 2$–1) observations were made with the NRAO 12 m telescope at Kitt Peak during 1991 May–June.

The beam size at 98 GHz is $\sim 70''$. The front end consisted of an SIS junction, dual polarization receiver with each polarization feeding a 128 channel, 100 kHz filter bank. The velocity resolution per channel was 0.31 km s^{-1}, and the total velocity coverage was nearly 40 km s^{-1}. The data were obtained in the frequency-switched mode with a frequency throw of ± 2 MHz. System temperatures on the sky varied from 400 to 700 K depending on elevation and weather conditions. Seventeen lines of sight were observed in MBM 40, and the results are listed in Table 3.

Traditionally, the lower rotational levels of CS have been considered tracers of high-density molecular gas (see, e.g., Snell et al. 1984). We thus observed 17 positions along the MBM 40 ridge in the CS ($J = 2$–1) transition. The observed positions are denoted in Figure 2 as filled circles for detections and crosses for nondetections. Of the 17 lines of sight, 11 yielded detections in three separate regions of the main ridge (Table 3). With the exception of positions A and B, the CS ($J = 2$–1) line does not correlate well with the H_2CO or even the CO observations. For instance, it is somewhat surprising that position Q produced only an rms noise value of 18 mK since this line of sight shows the strongest H_2CO 6 cm absorption over the entire cloud. However, the differing resolutions of the two sets of observations may indicate that clumping effects are significant and cannot be ignored. The only way to be certain that an anticorrelation exists between the two molecular species is to map the entire cloud in the CS ($J = 2$–1) line, an enterprise that currently requires prohibitive amounts of telescope time.

A significant CS concentration does exist centered at position K [$(\alpha:\delta) = (16^h08^m34^s:21°54'30'')$]. The incomplete mapping shows that the CS clump is at least $3' \times 4'$ in size (0.09 pc $\times$ 0.12 pc at the adopted cloud distance). The $W(^{12}CO)/W(^{13}CO)$ ratio is 4.8 at the center of this region and the ^{13}CO optical depth is 0.6 (see Table 2), indicative of rather substantial ^{13}CO column density. In light of this, it is surprising that a region with virtually identical ^{13}CO properties [at $(\alpha:\delta) = (16^h08^m20^s:22°02'00'')$] has only a 19 mK rms upper limit for the CS ($J = 2$–1) line. Similarly, position G shows CS emission, yet the $W(^{13}CO)/W(^{12}CO)$ ratio is 9, and the ^{13}CO optical depth is only 0.2. In these cases, clumping or sampling effects are not a problem because the CO and CS data have virtually the same angular resolution. It is likely that the above regions differ because of varying excitation conditions, but without more data we cannot speculate further.

TABLE 3

CS ($J = 2$–1) LINE PARAMETERS FOR MBM 40

Position	R.A. (1950)	Decl. (1950)	T_R^* (mK)	Δv (km s^{-1})	v_{LSR} (km s^{-1})
A	$16^h07^m54^s.4$	22°09′28″	56	0.35	3.25
B	16 07 54.4	22 11 28	77	0.70	2.77
C	16 08 12.0	22 00 00		25 mK rms	
D	16 08 20.0	22 02 00		19 mK rms	
E	16 08 24.0	21 55 00	61	0.26	3.31
F	16 08 24.0	21 57 00		13 mK rms	
G	16 08 24.0	21 59 00	76	0.38	3.31
H	16 08 30.0	21 54 30	68	1.30	3.69
I	16 08 30.0	21 57 00		17 mK rms	
J	16 08 34.0	21 53 30	63	0.53	3.37
K	16 08 34.0	21 54 30	95	0.62	3.46
L	16 08 34.0	21 55 30	96	0.56	3.39
M	16 08 38.0	21 53 30	77	0.67	3.28
N	16 08 38.0	21 54 30	117	0.55	3.35
O	16 08 38.0	21 55 30	128	0.36	3.32
P	16 08 44.0	21 54 30		34 mK rms	
Q	16 08 48.0	21 52 00		18 mK rms	

Although the presence of CS emission is normally considered evidence for dense molecular gas ($4 \leq \log n \leq 6$), the detection of CS ($J = 2$–1) emission in diffuse and translucent clouds (Drdla, Knapp, & van Dishoeck 1989) has revised this perception. Since the molecule has a large dipole moment, electron impacts are capable of populating the $J = 2$ level of the $v = 0$ ground state so that CS ($J = 2$–1) emission can be detected even from regions with densities less than 100 cm^{-3}. The translucent cloud models presented by Gredel et al. (1992) predict CS column densities in the range 1.1×10^{13}–1.2×10^{14} cm^{-3} depending on parameters such as the cloud density, sulfur depletion, and UV radiation field. Column densities in this range can produce observable radio lines according to Drdla et al. (1989) in gas that has densities as low as 500 cm^{-3} for electron abundances $(n_e/H_2) = 1 \times 10^{-4}$ and $T_K = 15$ K. Since we do not have an independent estimate of the electron abundance in the cloud, we cannot use our CS ($J = 2$–1) observations to determine the column densities in cores which have CS detections.

In summary, the CS evidence is ambiguous and does not prove or disprove the existence of low-mass cores in MBM 40. The ^{12}CO and ^{13}CO data, when coupled with the H_2CO 6 cm observations, imply that the molecular ridge region has a density of $\geq 10^3$ cm^{-3}, at least an order of magnitude lower than the low-mass cores described by Myers (1985).

2.2. *Is MBM 40 Gravitationally Bound?*

Despite the lack of conventional molecular cores, star formation in MBM 40 may still be possible given the recent scenarios that envision the formation of stars in relatively low-density gas (Dyson & Hartquist 1983; Lépine & Duvert 1994; Christodoulou & Tohline 1990). However, if a nonconventional star-forming scenario is relevant for MBM 40, it is may be relevant to determine if the molecular mass of the cloud is sufficient to produce a gravitationally bound object that can survive as an entity long enough for star formation to commence. The gravitational stability of the cloud can be determined to first order by comparing the magnitude of the gravitational potential and kinetic energy terms in the virial equilibrium equation. For a spherically symmetric, homogeneous cloud, the gravitational potential energy is given by

$$\Omega = -(\tfrac{3}{5})M^2GR^{-1}\,, \tag{1}$$

while the kinetic energy term is

$$T = 2\pi\sigma_i^2\mu m_H nR^3\,, \tag{2}$$

where σ_i is the one-dimensional internal velocity dispersion of the gas ($=0.25$ km s^{-1}; MBM), μ is the molecular weight, m_H is the mass of the hydrogen atom, n is the average density, M is the mass, and R is the radius of the cloud. With an estimate of the cloud mass, the two terms can be evaluated and compared. We use two independent techniques to obtain the mass of MBM 40: first, we utilize a CO–H_2 conversion factor; our second method uses infrared observations and the standard gas-to-dust ratio.

2.2.1. *The Mass of the Cloud from CO Data*

The mass of a cloud can be determined directly from CO data, if a suitable conversion factor from W(CO) to the

primary constituent of the cloud (H_2) can be found. This conversion factor is commonly referred to as the "X" factor or X_{CO} and, for the Galactic molecular cloud ensemble, is often taken to range from 2 to 4×10^{20} cm^{-2} [K km s^{-1}]$^{-1}$ (the units will be dropped hereafter for brevity). Magnani & Onello (1995) have pointed out the pitfalls of applying a "standard" X_{CO} factor to translucent clouds. They suggest that the best technique for determining X_{CO} in translucent clouds is to calibrate the ratio for a particular cloud using observations of the CH hyperfine ground state transition at 3335 MHz. Such a calibration for MBM 40 has been made (Magnani et al. 1996b) and yields a value of 1.8×10^{20}. Along the MBM 40 molecular ridge, five separate measurements of the X-factor produced values ranging from 0.8 to 2.0×10^{20}—a rather limited range given the variations usually encountered in translucent clouds (Magnani & Onello 1995). The average value compares favorably with the average value obtained in Table 2 using $N(H_2)$ derived from the ^{13}CO data and W(CO) from Magnani et al. (1988): 0.7×10^{20}. Since Magnani & Onello (1995) determine that the CH method is the most reliable one for translucent clouds, for the remainder of this paper, we use 1.8×10^{20} as the value for X_{CO} in MBM 40.

We express the mass of the cloud in terms of readily available parameters with the equation

$$M = 5.8 \times 10^{-3} A d^2 N_{21} M_{\odot} , \quad (3)$$

where A is the area of the cloud in square degrees, d is the distance in pc, and N_{21} is the average H_2 column density in units of 10^{21} cm^{-2}. The average W(CO) for MBM 40 is 2.0 K km s^{-1} (MBM), so that $X_{CO} = 1.8 \times 10^{20}$ yields an average value of $N_{21} = 0.12$. The area of the cloud is 0.7 deg^2 so that, based on the preceding assumptions, the mass of MBM 40 is $\sim 15\ M_{\odot}$. If we correct for the presence of He in the cloud, the overall mass increases to $\sim 19\ M_{\odot}$.

2.2.2. *The Mass of the Cloud from Infrared Observations*

An alternative derivation of the mass of MBM 40 can be made using optically thin infrared observations to determine the mass of the cloud and then scaling to a total mass by an adopted gas-to-dust ratio. Figure 3 is a 100 μm *IRAS* image of MBM 40 and its immediate environment. Infrared images of high-latitude molecular clouds do not at first glance look noticeably different from infrared atomic cirrus clouds. The distinction between atomic and molecular cirrus seems to be a gradual transition to a regime of column density and pressure that allows clouds to contain significant quantities of molecular gas (Elmegreen 1993). The visual extinction through molecular cirrus is somewhat higher than for atomic clouds, which is how these regions were selected for observation in the original MBM survey. Also, a comparison of all-sky surveys in IR and H I emission identifies molecular cirrus as regions of enhanced IR/HI, presumably because there is additional dust associated with gas in the form of H_2 (Désert, Bazell, & Boulanger 1988; Blitz, Bazell, & Désert 1990). It is now believed that molecular cirrus clouds are more condensed features embedded in larger arcs of H I (see, e.g., Gir, Blitz, & Magnani 1994). In the case of MBM 40, the puffs of cirrus emission seen in Figure 3 lie in an arc that extends roughly 6° and are otherwise isolated. Although the adjacent cirrus clouds have not

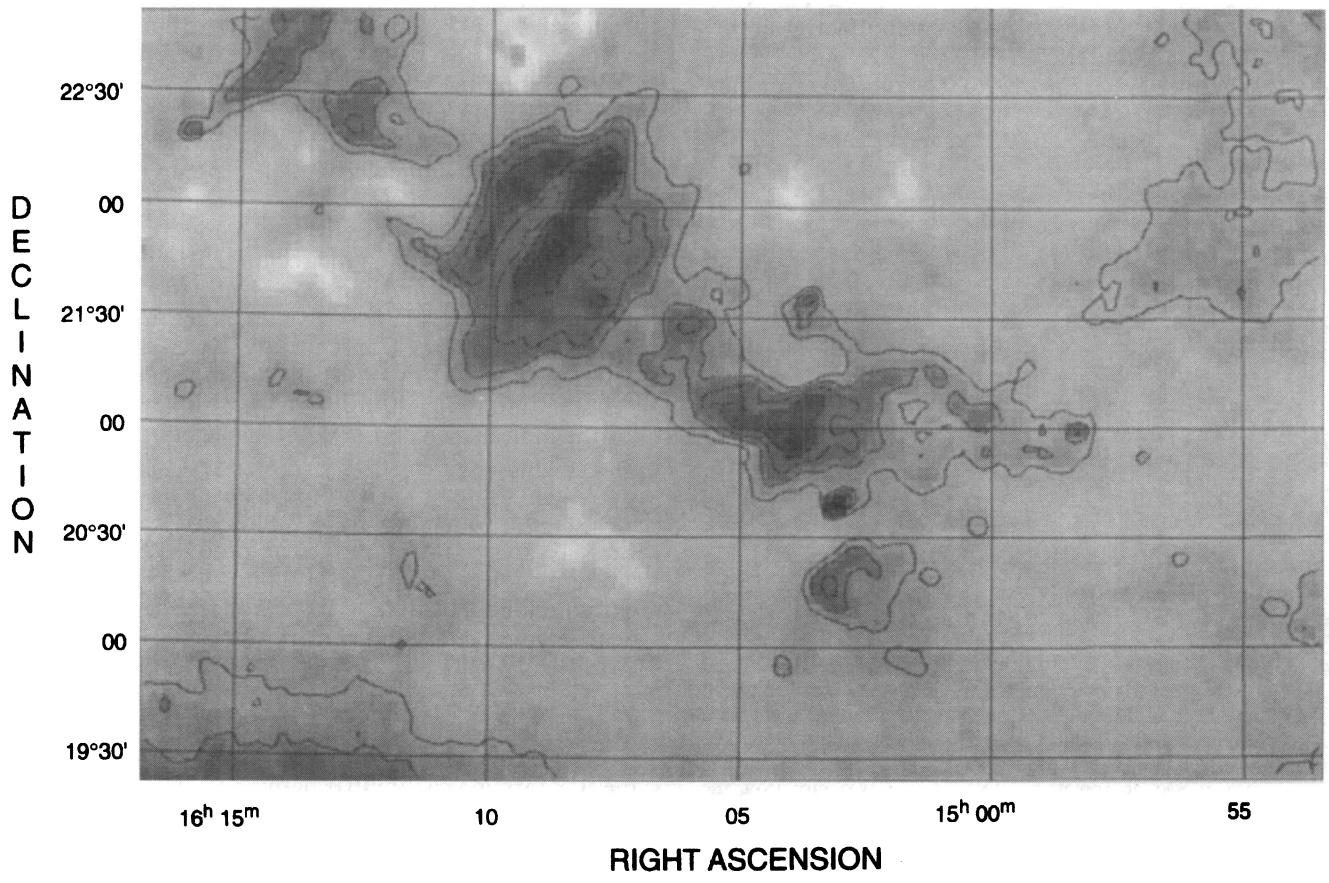

FIG. 3.—A 100 μm map of the environs of MBM 40. The contour levels are set at 1.7, 2.3, 3.0, 3.9, and 5.0 MJy sr^{-1}.

been covered by the existing CO maps of MBM 40 (MBM; de Vries 1988), they are probably atomic because they are not noticeable on the POSS plates as reflection nebulosities and are not tabulated as having excess IR/H I (Désert et al. 1988). The cirrus clouds to the upper left and lower right of MBM 40 in Figure 3 probably have peak column densities that are lower by a factor of ~ 0.55 and 0.75, respectively, since these are the factors by which their peak 100 μm surface brightnesses are reduced compared to MBM 40.

The infrared flux of the MBM 40 region was obtained from *IRAS* Sky Flux Plate Images (HCON 1) at 100, 60, 25, and 12 μm. The images were taken from a survey of the infrared properties of molecular cirrus (Verter et al. 1996), and the data reduction procedures used in the survey are described by Verter & Rickard (1996). At each wavelength, the image background was fitted with a tilted plane and subtracted. The MBM 40 cloud flux was integrated inside the 0.33 K km s^{-1} contours of the MBM CO ($J = 1$–0) map. The cloud emission was measured as a difference against the residual off-cloud emission in the background-subtracted image. This step is necessary because cirrus clouds are so faint that residuals in the background subtraction can be comparable to the cloud emission (Verter & Rickard 1996).

Figure 4 is a plot of the MBM 40 integrated emission versus *IRAS* wave band. Although the cloud was barely a smudge on the background-subtracted images at 25 and 12 μm, the difference against neighboring off-cloud areas produced a detectable flux. The propagated measurement uncertainty is basically a function of the rms pixel dispersion divided by the number of resolution elements in the measurement area for both the on- and off-source areas. The *IRAS* detectors are also afflicted by intrinsic gain uncertainties, which introduce a fixed photometric uncertainty of 16, 13, 13, and 12% at 100, 60, 25, and 12 μm, respectively (Verter & Rickard 1996). The plotted error bars in Figure 4 are the net result of combining measurement and photometric uncertainties.

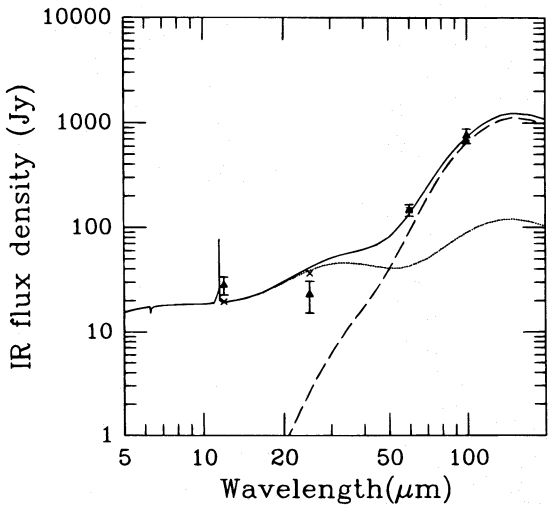

FIG. 4.—Infrared flux density of MBM 40 vs. wavelength. The reduced data are plotted as solid triangles centered on the nominal wavelengths of the *IRAS* filters. Each of these points represents the net infrared emission of the background-subtracted cloud image, integrated within the 0.33 K km s^{-1} contours of the MBM CO (1–0) map. The error bars include both measurement and photometric uncertainties. For comparison, the cross at each *IRAS* nominal wavelength is the convolution of the model emission with the *IRAS* filter. The solid curve plots emission versus wavelength for the best fit of the Dwek grain model; dashed and dotted lines show the contributions of MRN grains and stochastically heated grains, respectively.

The dust mass of MBM 40 can be determined by fitting a grain model to the integrated fluxes in the four *IRAS* wave bands. Most of the dust mass in the clouds is in grains with size between 0.025 and 0.25 μm, which radiate at an equilibrium temperature and give rise to most of the 60 μm and 100 μm emission. This grain population is well described by the standard "MRN" dust model (Mathis, Rumpl, & Nordsieck 1977), and assuming that all the 60 and 100 μm *IRAS* emission originates from these grains, we derive a dust mass of 0.073 $M_\odot$ within the lowest CO contour in the MBM map.

Additional mass is contributed by stochastically heated dust grains and macromolecules (PAHs, QCCs, HACs) that are the source of the "overidentified" near-infrared continuum and emission features (see, e.g., § II in Allamandola & Tielens 1989).

Our approach is to fit simultaneously the MBM 40 fluxes at 100, 60, 25, and 12 μm by adopting a modified MRN grain model in which the grain size distribution for graphite becomes much steeper below ≈ 200 Å, introducing large numbers of very small particles that undergo stochastic heating. This approach was developed by Dwek (1986), among others, and applied to three molecular cirrus clouds by Weiland et al. (1986); we have used more recent versions of these models. The three free parameters in this model are (1) the grain size at which the size distribution changes exponent (which must be less than ~ 200 Å where stochastic emission sets in), (2) the minimum grain size (which must be greater than 3 Å to resist sublimation, and (3) the steepness of the enhanced size distribution (which must be greater than the MRN exponent -3.5). The fits with the lowest χ^2 values allow 0.057–0.109 $M_\odot$ of dust within the lowest CO contour of MBM with a best fit of 0.095 $M_\odot$. If we now scale up the dust mass by a gas-to-dust value of 100, we obtain a best-fit mass for MBM 40 of 9.5 $M_\odot$. Given the uncertainty in the gas-to-dust ratio, the agreement with the mass obtained from molecular spectroscopy considerations is good.

However, as the infrared map in Figure 3 makes clear, there is more emission in the region than what was mapped by MBM. The infrared emission identifiable with the MBM 40 cloud subtends an area 2.1 times larger than that covered by the CO contours. Consequently, if we scale up the mass determined for MBM 40 from the molecular data to the "entire" infrared-emitting region, we obtain a best estimate for the molecular cloud of 40 $M_\odot$. We adopt this value for the remainder of the paper.

With an estimate of 40 $M_\odot$ for the cloud mass, Ω and T in equations (1) and (2) have values of 6.4×10^{43} ergs and 4.2×10^{43} ergs, respectively. The ratio of T/Ω (~ 1) is significantly lower than typical values for translucent high-latitude clouds (10–100; MBM) and indicates that MBM 40 is an atypical low-extinction translucent cloud. The similarity between Ω and T for MBM 40 indicates that the cloud is not breaking up on a sound-crossing timescale and may be stable for timescales long enough for star formation to occur. This is one of the reasons we chose to investigate the star-forming capabilities of this particular cloud.

With the cloud mass, we can estimate the expected star formation efficiency of MBM 40 *if* the rate were similar to that in the Taurus-Auriga dark clouds. The total mass of the Taurus-Auriga dark clouds is 3.5×10^4 $M_\odot$

(Ungerechts & Thaddeus 1987). Kenyon & Hartmann (1995) estimate the minimum number of PMS members of Taurus-Auriga to be ~200, while the *ROSAT* All-Sky survey has revealed as many as $\sim 10^3$ TTS candidates (Neuhäuser et al. 1995b); hence, the star formation efficiency probably lies somewhere between 1% and 3%. This shows that in a 40 $M_\odot$ cloud, one can expect up to several T Tauri stars with a few 0.1 $M_\odot$ each.

3. RESULTS OF THE X-RAY/OPTICAL SEARCH

3.1. *The ROSAT Observations*

One of the best methods for identifying PMS stars is via their X-ray emission (see, e.g., Walter et al. 1988; Alcalá et al. 1995; Neuhäuser et al. 1995c). The X-ray data for this study were acquired via two methods which employed the *ROSAT* Position Sensitive Proportional Counter (PSPC). Briefly, the PSPC had a field of view ~2° in diameter, sensitivity to ~0.1–2.4 keV X-rays, on-axis spatial resolution of ~40″ in the survey mode and ~20″ in pointed mode, and spectral resolution of $\Delta E/E \sim 43\%$ at 0.93 keV (Zimmermann et al. 1993).

One method of observing MBM 40 utilized the *ROSAT* All-Sky Survey and was carried out between 1990 July and 1991 August. The telescope, with the PSPC at the focal plane (Trümper 1983; Pfeffermann et al. 1986) scanned the sky once per satellite orbit along great circles containing the north and south ecliptic poles. X-ray sources were typically visible for ~20–30 s per scan. Since the visibility of an object depends on its ecliptic coordinates, the sources in MBM 40 ($\beta \sim 41°$) were observed for an exposure time of ~550–650 s. We examined a 3°.5 × 6°.5 area centered on the CO emission peak of MBM 40 (Fig. 5). All of the source detection analysis was performed using the NOV93 version of the Extended Scientific Analysis Software System (EXSAS) software developed at the Max-Planck-Institut für Extraterrestrische Physik (MPE; Zimmermann et al. 1993).

We conducted our analysis in a manner similar to that performed by Neuhäuser et al. (1995a). We searched for sources using the EXSAS LDETECT, MDETECT, and MAXLIK algorithms. The LDETECT algorithm uses a "sliding-window" technique, which utilizes a local background that surrounds the detection cell. The major advantage of this method is that LDETECT is virtually independent of external parameters (such as background rate and distribution). However, since the local background is estimated only in a relatively small cell, this method is less sensitive than others that use the total field of view. The MDETECT algorithm uses a full field-of-view map of the expected instrumental background (modeled from actual parameters such as satellite orbit, solar aspect angle, and anticoincidence rates) in conjunction with photon and particle background estimates as the background against which the "sliding-window" technique is used. The source lists that are generated by these two algorithms are then subjected to a maximum likelihood analysis (MAXLIK) that fits the observed distribution of source counts to a source model (usually a flat background across the region of interest) and a point source (with a point-spread function appropriate for the source position in the field). The best fit is the most likely value for the background and source strength, as well as source position, given the observed distribution of counts. More detailed descriptions can be found in papers by Cruddace, Hasinger, & Schmitt (1988) and Zimmermann et al. (1993).

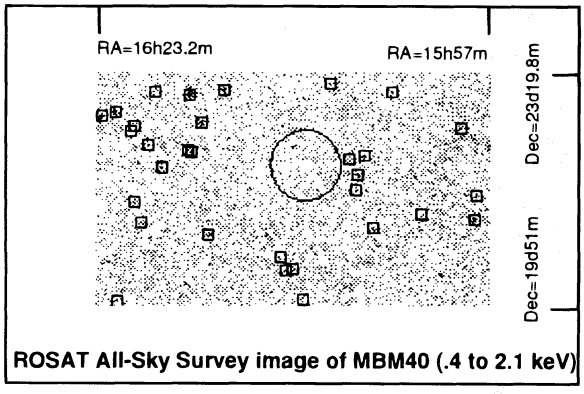

FIG. 5.—*ROSAT* All-Sky Survey hard-band (0.5–2.0 keV) map of the region centered on MBM 40. The small squares indicate the locations of the 31 sources, while the large circle indicates the location of the *ROSAT* pointed observation shown in Fig. 6. The fact that many sources indicated on this hard-band image cannot be recognized as sources is a result of their being detected in the soft band only, indicating that they are not T Tauri stars, but, rather, are either dMe stars or quasars.

Our search was conducted in different *ROSAT* standard "bands," defined as follows: "*S*" = 0.1–0.4 keV; "*H*" = 0.5–2.0 keV; "H_1" = 0.5–0.9 keV; "H_2" = 0.9–2.0 keV; "*B*" = 0.1–2.4 keV. After merging the LDETECT and MDETECT source lists from all different bands, the merged source list was again tested with MAXLIK; the maximum likelihood threshold was $ML = 8$. An additional utility of the bands is that "hardness ratios," somewhat analogous to optical photometric colors, can be defined. Since the cross section for absorption of X-rays by the interstellar medium is well understood (Morrison & McCammon 1983), these hardness ratios allow us to make inferences about the amount of absorbing material along the lines of sight toward the sources detected (Neuhäuser et al. 1995a).

Again we have employed standard *ROSAT* definitions of hardness ratios:

$$HR_1 = \frac{Z_H - Z_S}{Z_H + Z_S}, \tag{4}$$

$$HR_2 = \frac{Z_{H_2} - Z_{H_1}}{Z_H}, \tag{5}$$

where Z_H, Z_S, Z_{H_2}, and Z_{H_1} represent the count rates in each of the bands.

We combined the individual source lists, merging sources from different energy bands which lay within 1′ of each other. A total of 31 sources were detected in the All-Sky Survey. The number of sources per deg^2 in MBM 40 at this sensitivity level is somewhat smaller than that indicated by the log *N*–log *S* relation found from a deep *ROSAT* survey of the Lockman Hole conducted by Hasinger et al. (1993); this diminution is most likely attributable to the extinction in the line of sight toward MBM 40 ($A_V < 2$ mag), since the Galactic latitudes of both objects are roughly the same. Nevertheless, this could be interpreted as an initial indication that there are no X-ray emitting PMS stars in MBM 40.

The second method of observing MBM 40 involved the pointed phase of the mission. A 7.3 ks PSPC observation of MBM 40, centered on $(\alpha:\delta) = (16^h09^m09^s.6:22°03'00'')$ and covering the densest region of the cloud (the PSPC field of

view is 2° in diameter), was performed on 1993 August 18–19 and is shown in Figure 6; the investigators for this observation, David Burrows and collaborators, had proposed the observation in order to study the possible shadowing of the X-ray background by MBM 40. They kindly allowed us access to the data in order to study any point sources that might have been detected. Although the standard *ROSAT* data products include a "Master" source list, we have chosen to confirm the entries on that list (and perhaps to find additional sources) by reanalyzing the data. Our analysis procedures for the pointed data differed from those utilized for the All-Sky Survey data. In particular, the X-ray source list for the pointed image was derived using the IRAF/PROS LDETECT routine. This detection routine was run for each of the nine possible combinations of cell size with energy band (three cell sizes and three energy bands) in order to find candidate sources above a signal-to-noise ratio threshold S/N = 2.5. We take S/N to be the ratio between the net source counts (see below), S, divided by the 1 σ error in S, σ_S (see, e.g., Gagné & Caillault 1994). This generated nine possible source lists. The LMATCHSRC routine was then run to merge redundant sources appearing on more than one list; the spatial separation criterion for merger was that the sources had to have positions within their respective 3 σ positional error circles (as determined by the LMATCHSRC routine). We then confirmed (or refuted) the existence of the sources by visual inspection of the image; at the same time, we inspected the image for any sources that may have been missed by the LDETECT routine: four additional sources with S/N > 2.5 were found.

In order to measure the flux from the pointed observation sources, we utilized source circle radii calculated from the *ROSAT* off-axis, energy-dependent point response function (found in the *ROSAT* Mission Description); these radii include 99% of the source photons. Local background counts were calculated from a concentric annulus, where the inner radius was twice as large as the source circle radius and the outer radius 200 pixels (~100″) larger than the inner radius. Sources were "masked" from the image when the local background was calculated so that background counts were not overestimated. Our final, "pointed" source list consists only of sources with S/N > 2.5 in the broad energy band. A total of 14 sources were detected in the pointed observation, only one of which was found in the survey.

There are no cataloged PMS stars in this region of the sky. Using an X-ray error radius of ~40″ (Neuhäuser et al. 1995a), we cross-referenced all 44 of our X-ray sources with the SIMBAD, NED, and *IRAS* Faint Source databases to remove any extragalactic objects from our list of candidates for follow-up optical spectroscopy; four objects were elimi-

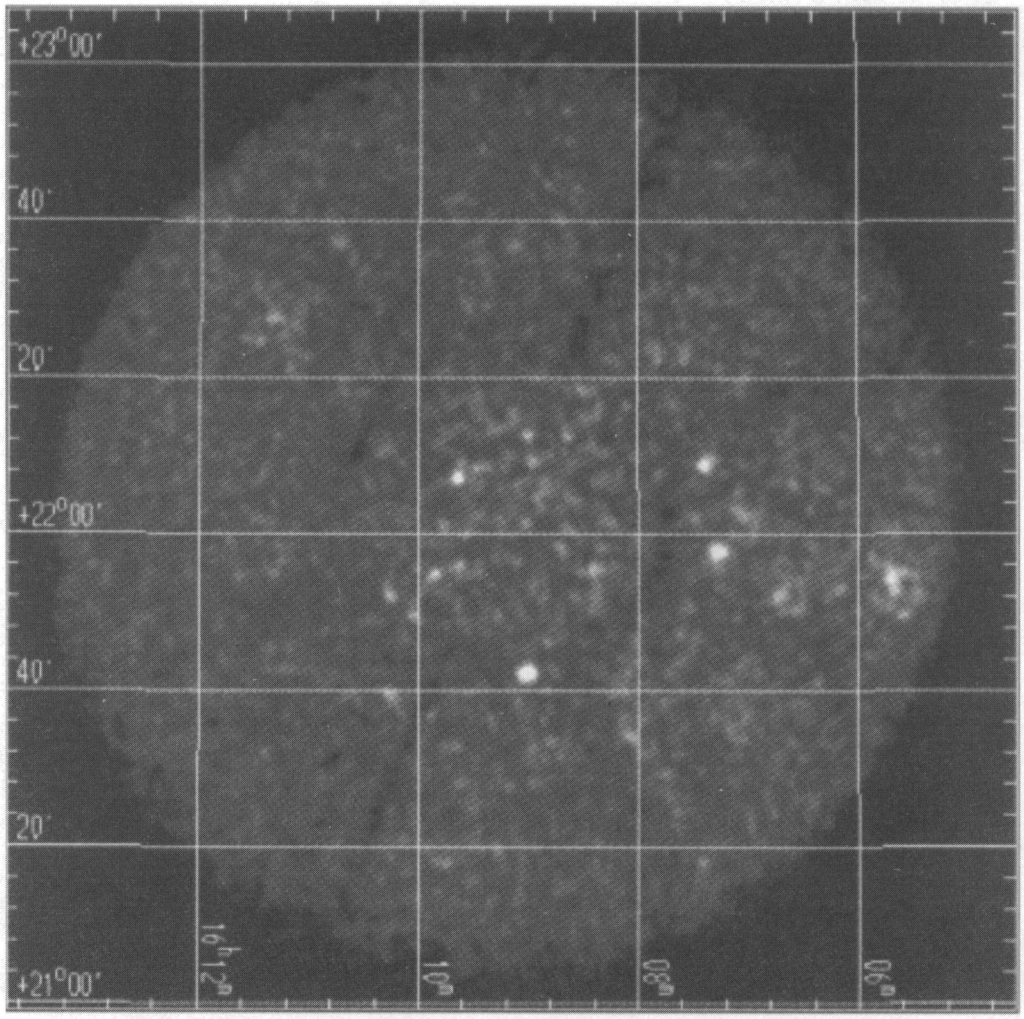

FIG. 6.—Broadband (0.1–2.4 keV) X-ray image of the 7.3 ks *ROSAT* PSPC pointed observation of MBM 40

nated via this procedure. Visual magnitudes for the remainder were obtained from SIMBAD (when available) or were determined, within 0.25 mag, from visual inspection of the POSS prints.

ROSAT-detected T Tauri stars can be distinguished from *ROSAT*-detected non–T Tauri stars by hardness ratios (Neuhäuser et al. 1995b). This allows us to eliminate two of our sources as candidates for being PMS stars; their HR_2 values $= -1$, far outside the range of acceptable values. Although this discrimination technique appears to work sufficiently well for discovering new T Tauri stars (from follow-up observations of previously unidentified *ROSAT* survey sources), it is certainly helpful to use additional criteria to select T Tauri candidates. One such additional criterion is the X-ray–to–optical flux ratio. Maccacaro et al. (1988) point out that X-ray sources with Galactic and extragalactic counterparts can be separated at a high confidence level (>90%) prior to any optical spectroscopy. Results of the *Einstein* Extended Medium Sensitivity Survey (EMSS) show that among extragalactic sources all but a few have $\log (f_X/f_v) > -1.0$; in addition, those few are normal galaxies which are easy to identify on the POSS plates. With the exception of dMe stars, all stars, including the T Tauri stars observed in the *Einstein* EMSS, have $\log (f_X/f_v) < -1.0$ (Stocke et al. 1991). Since we are looking for X-ray–active low-mass PMS stars and in many cases are making rough estimates of the visual magnitude as seen on the POSS plates, we have adopted a more conservative cutoff. We consider sources that have $\log (f_X/f_v) > 0.0$ to be extragalactic and those with $\log (f_X/f_v) < 0.0$ to be possible stellar candidates. These values are calculated from:

$$\log (f_X/f_v) = \log B + 0.4V - 5.08 , \quad (6)$$

where B is the *ROSAT* broadband count rate and V is the optical counterpart's visual magnitude (Sterzik et al. 1995). Given the errors in the measured X-ray flux and the estimated visual magnitudes, the maximum error in our estimate of $\log (f_X/f_v)$ is ~ 0.5. Thirteen sources were identified as extragalactic via this method. These, along with the six sources previously mentioned, were eliminated from further consideration. The remaining 25 objects plausibly have stellar optical counterparts.

These 25 X-ray sources and their 33 associated optical counterparts (within the X-ray error radius of $\sim 40''$) are listed in Table 4. Those from the All-Sky Survey (17 sources = 22 optical candidates) appear in the upper half of the table, while the eight (=11 optical candidates) from the pointed observation appear in the bottom half. We list the source name and position, existence maximum likelihood (for survey sources) or S/N ratio (for pointed observation sources), broadband count rate and 1 σ error, and the two hardness ratios and their 1 σ errors in the first seven columns. In Figure 7 we plot the HR_2 values versus the HR_1 values for these 25 X-ray sources; all except two of them have HR_1 values that are positive, and all but one have HR_2 values > -0.5. Since PMS stars are located in the same upper right-hand portion of such plots (Neuhäuser et al. 1995a), the hardness ratio data for our X-ray sources are generally consistent with the possibility of their being PMS stars.

Another advantage to having calculated the hardness ratios is that one can determine the dereddened X-ray fluxes of the sources via the technique described by Neuhäuser et al. (1995a). The method essentially assumes that the observed energy distribution depends only on the hydrogen column density and the temperature of a single-temperature Raymond-Smith thermal plasma (Raymond & Smith 1977). Since the observed energy distribution is expressed by hardness ratios, any pair of HR_1, HR_2 values corresponds to a pair of T, N_H values. Together with the PSPC energy response matrix, the energy conversion factor, and the count rate, the best-fit T, N_H pair yields a corrected X-ray flux; these values and their errors are listed in column (8) of Table 4. Count rates used to calculate the flux ratios with equation (6) are not dereddened but, rather, observed count rates, in order to compare correctly with the flux ratio limits given by Stocke et al. (1991) who also use fluxes which are not dereddened.

Since the two observing methods had very different exposure times, the resulting sensitivities were correspondingly different: a threshold limiting flux of $\sim 10^{-13}$ ergs cm^{-2} s^{-1} was achieved during the All-Sky Survey, while the pointed observation was ~ 10 times more sensitive. These values correspond to minimum X-ray luminosities of $\sim 10^{29.1}$ and $\sim 10^{28.1}$ ergs s^{-1} at the adopted distance of MBM 40.

Despite the fact that the deeper, pointed observation's field of view was included in the All-Sky Survey region analyzed, only one source, RXJ 1605.6+2153, was detected by both methods. Actually, this is not too surprising, since the All-Sky Survey should detect only the brightest sources, which, all else being equal, should not appear in the region of higher extinction where the pointed observation was made. The candidate RXJ 1605.6+2153 was detected on the periphery of the field of view of the pointed observation. However, its location produced a poorly determined source position relative to that of the All-Sky Survey so that we list only RXJ 1605.6+2153 in the upper portion of Table 4.

In columns (9) and (10) of Table 4 we list the optical counterparts' apparent magnitudes and f_X/f_v ratios. Approximately half of the optical counterparts have visual magnitudes brighter than 15.5, the limit to which we obtained optical spectra. In the next section, we describe the optical observations of these brighter candidates.

3.2. *The Mount Hopkins Observations*

Our spectra were obtained during 1994 May and July and 1995 March using the FAST spectrograph with the 600 lines mm^{-1} grating of the 1.5 m Fred Lawrence Whipple Observatory telescope. The wavelength range of the spectra is $\sim$5590–7590 Å; the slit size of 1.″5 provided a reciprocal dispersion of 0.75 Å pixel^{-1}. The spectra were bias corrected and then divided by the appropriate flat field. Wavelength calibration was performed by comparison with standard He-Ar and Ne spectra. All optical data reduction was performed using standard IRAF routines.

Integration times of 2 minutes for sources brighter than $V \sim 10$, 6 minutes for sources brighter than $V \sim 13$, and 10 to 15 minutes for fainter sources produced spectra with $\langle S/N \rangle \sim 30$. The 3 σ equivalent width was determined from EW $= 3\Delta\lambda/(S/N)$ Å. Using our 2 pixel resolution, S/N ~ 22 for the 600 lines mm^{-1} grating is required to detect a line with an EW of 0.2 Å at a 3 σ confidence level.

Spectral types were determined by comparison to spectral standard stars and via comparison with the spectral atlas compiled by Allen & Strom (1995). The assigned spectral types and the EWs of the Hα emission appear in columns (11)–(12) of Table 4. Negative equivalent widths represent Hα emission.

TABLE 4

X-RAY POINT SOURCES NEAR MBM 40 WITH POSSIBLE STELLAR OPTICAL COUNTERPARTS

Name	RA 2000	Dec 2000	EXI_ML	Count Rate ct s^{-1}	HR1	HR2	X-ray flux $f_x/10^{-12}$ cgs	m_v	$\log(f_x/f_v)$	SpT	$W(H_\alpha)$ Å
RXJ1557.7+2132	15:57:48.0	+21:32:56.2	9.1	0.014 ± 0.006	$+0.62 \pm 0.39$	$+0.91 \pm 0.42$	$0.341^{+0.148}_{-0.200}$	16.8	-0.21	...	...
RXJ1558.7+2235	15:58:46.2	+22:35:37.7	17.2	0.015 ± 0.006	$+0.63 \pm 0.32$	$+0.56 \pm 0.30$	$0.172^{+0.116}_{-0.091}$	17.1	-0.06	...	...
RXJ1601.4+2116	16:01:27.2	+21:16:08.1	22.1	0.035 ± 0.010	-0.35 ± 0.29	$+0.47 \pm 0.70$	$0.319^{+0.550}_{-0.177}$	15.0	-0.53	M3	-6.03
RXJ1604.6+2103a	16:04:40.0	+21:03:36.3	31.6	0.053 ± 0.012	-0.31 ± 0.22	-0.52 ± 0.35	$0.357^{+0.493}_{-0.103}$	13.4	-0.99	M1	-4.47
RXJ1604.6+2103b								15.1	-0.31	M3	-7.31
RXJ1605.2+2210	16:05:15.5	+22:10:53.4	25.4	0.028 ± 0.008	$+1.00 \pm 0.13$	$+0.08 \pm 0.28$	$0.271^{+0.155}_{-0.096}$	8.3	-3.31	F8	2.08
RXJ1605.6+2153	16:05:37.9	+21:53:38.5	30.8	0.053 ± 0.012	$+0.19 \pm 0.23$	$+0.08 \pm 0.27$	$0.462^{+0.126}_{-0.123}$	7.1	-3.51	G0III	3.91
RXJ1607.4+2319a	16:07:26.9	+23:19:09.2	8.3	0.008 ± 0.004	$+1.00 \pm 0.25$	$+0.84 \pm 0.41$	$0.211^{+0.106}_{-0.163}$	15.6	-0.91	...	...
RXJ1607.4+2319b								17.5	-0.15	...	...
RXJ1610.8+2036	16:10:52.6	+20:36:56.7	9.1	0.016 ± 0.007	$+0.23 \pm 0.45$	$+0.27 \pm 0.52$	$0.143^{+0.138}_{-0.071}$	15.0	-0.87	G8	1.84
RXJ1615.6+2057a	16:15:39.1	+20:57:46.9	9.0	0.015 ± 0.006	$+0.67 \pm 0.40$	$+0.50 \pm 0.16$	$0.349^{+0.149}_{-0.213}$	14.5	-1.12	G8	2.03
RXJ1615.6+2057b								16.1	-0.48	...	...
RXJ1616.1+2241	16:16:09.6	+22:41:09.4	48.9	0.051 ± 0.011	$+1.00 \pm 0.03$	$+0.30 \pm 0.19$	$0.583^{+0.208}_{-0.201}$	14.9	-0.41	F8	2.89
RXJ1616.8+2215	16:16:50.0	+22:15:03.6	11.3	0.014 ± 0.006	$+0.42 \pm 0.36$	$+0.44 \pm 0.42$	$0.103^{+0.092}_{-0.059}$	16.6	-0.29	...	...
RXJ1619.3+2310	16:19:20.9	+23:10:14.5	8.1	0.007 ± 0.004	$+1.00 \pm 0.27$	$+0.09 \pm 0.27$	$0.183^{+0.102}_{-0.128}$	16.4	-0.65	...	...
RXJ1620.0+2108	16:20:05.3	+21:08:01.1	14.0	0.034 ± 0.011	$+0.31 \pm 0.29$	-0.04 ± 0.34	$0.277^{+0.112}_{-0.118}$	6.0	-4.15	G8IIIb	1.90
RXJ1620.5+2126	16:20:34.6	+21:26:50.2	9.6	0.010 ± 0.005	$+0.50 \pm 0.47$	$+0.61 \pm 0.64$	$0.106^{+0.126}_{-0.069}$	15.6	-0.84	...	...
RXJ1620.6+2237	16:20:40.6	+22:37:59.9	14.5	0.013 ± 0.006	$+1.00 \pm 0.18$	$+0.03 \pm 0.42$	$0.126^{+0.116}_{-0.059}$	17.2	-0.07	...	...
RXJ1622.0+2250a	16:22:00.9	+22:50:17.2	168.3	0.184 ± 0.020	$+0.14 \pm 0.11$	$+0.14 \pm 0.14$	$1.660^{+0.445}_{-0.261}$	11.5	-1.21	M0	-2.50
RXJ1622.0+2250b								13.6	-0.37	G8	1.80
RXJ1622.8+2246a	16:22:55.0	+22:46:06.8	100.9	0.088 ± 0.014	$+0.69 \pm 0.13$	$+0.32 \pm 0.14$	$0.889^{+0.458}_{-0.238}$	10.1	-2.10	K0	1.67
RXJ1622.8+2246b								14.2	-0.46	K5	...
			S/N								
RXJ1606.7+2152	16:06:42.8	+21:52:02.9	4.4	0.020 ± 0.004	$+0.61 \pm 0.26$	$+0.16 \pm 0.19$	$0.170^{+0.078}_{-0.045}$	15.7	-0.50	F9	1.90
RXJ1607.3+2157a	16:07:16.9	+21:57:20.3	6.1	0.016 ± 0.003	$+1.00 \pm 0.27$	$+0.21 \pm 0.15$	$0.167^{+0.053}_{-0.048}$	15.6	-0.64	...	...
RXJ1607.3+2157b								17.1	-0.04	...	...
RXJ1609.0+2212	16:09:01.1	+22:12:33.2	2.6	0.002 ± 0.001	$+0.50 \pm 0.41$	$+0.40 \pm 0.42$	$0.024^{+0.018}_{-0.013}$	17.1	-0.90	...	...
RXJ1609.6+2156a	16:09:37.1	+21:56:06.9	2.5	0.002 ± 0.001	$+1.00 \pm 0.75$	$+0.22 \pm 0.46$	$0.020^{+0.024}_{-0.010}$	15.9	-1.42	...	...
RXJ1609.6+2156b								18.6	-0.34	...	...
RXJ1609.6+2207	16:09:39.1	+22:07:04.5	4.4	0.005 ± 0.001	$+1.00 \pm 0.35$	$+0.19 \pm 0.25$	$0.048^{+0.031}_{-0.017}$	14.8	-1.5	K0	1.84
RXJ1609.8+2154a	16:09:51.3	+21:54:55.8	2.8	0.003 ± 0.001	$+1.00 \pm 0.63$	-0.18 ± 0.39	$0.024^{+0.021}_{-0.011}$	17.6	-0.56	...	...
RXJ1609.8+2154b								18.5	-0.20	...	...
RXJ1610.2+2139	16:10:16.5	+21:39:31.7	2.6	0.005 ± 0.002	$+1.00 \pm 0.73$	-0.13 ± 0.39	$0.048^{+0.043}_{-0.023}$	18.4	-0.02	...	...
RXJ1611.3+2227	16:11:19.2	+22:27:30.0	3.0	0.013 ± 0.004	$+0.10 \pm 0.34$	$+0.40 \pm 0.40$	$0.122^{+0.073}_{-0.046}$	16.9	-0.21	...	...

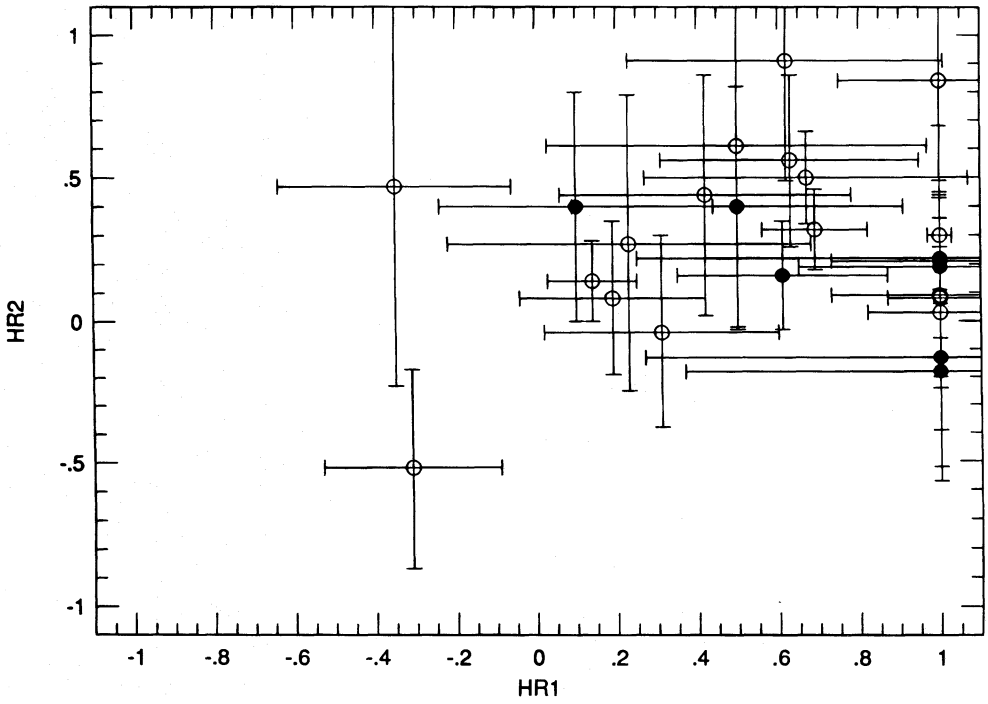

FIG. 7—Plot of the X-ray hardness ratios HR_2 vs. HR_1. Open circles represent sources detected in the *ROSAT* All-Sky Survey; filled circles represent sources detected in the pointed observation. One sigma error bars are indicated.

Our search for evidence of PMS stars in MBM 40 revealed four stars that exhibited Hα emission (EW ~ 5 Å), but none of these objects showed statistically significant Li absorption. The broadband spectra (5700 Å to 7500 Å) of all four objects are shown in Figure 8, while in Figure 9, we show a close-up view of the 6550 Å to 6725 Å region. The fact that the gravity sensitive features in our spectra (e.g., the Na I D doublet and the Ca H band at 6370 Å) are quite strong suggests that these stars are indeed dwarfs and are not young (low-gravity) PMS stars. Since the Hα-emitting stars all have spectral type M, we expect that these stars are probably dMe stars along the line of sight toward MBM 40. Extrapolating from the Gliese & Jahreiss (1988) catalog of stars within 25 pc to the ~100 pc distance of MBM 40, we estimate that there should be ~5 dMe stars within the 3°.5 × 6°.5 area surveyed, consistent with our spectroscopic results. The estimated magnitudes and spectral types, together with the extinction along the line of sight, provide distance estimates to these M dwarfs, which, in turn, allow us to calculate their X-ray luminosities. We find that these four dMe stars have L_X values that place them in the same range (a few times 10^{29} ergs s^{-1}) as the X-ray–selected sample from the *Einstein* Medium Sensitivity Survey (Fleming et al. 1988). Although PMS models predict that early M dwarfs burn their lithium by an age of 10 Myr and, hence, that these stars could have been born in or near MBM 40 but be >10 Myr old, we feel that the field star explanation is more likely.

A similar analysis of *ROSAT* all-sky observations of the Taurus dark clouds was performed by Neuhäuser et al.

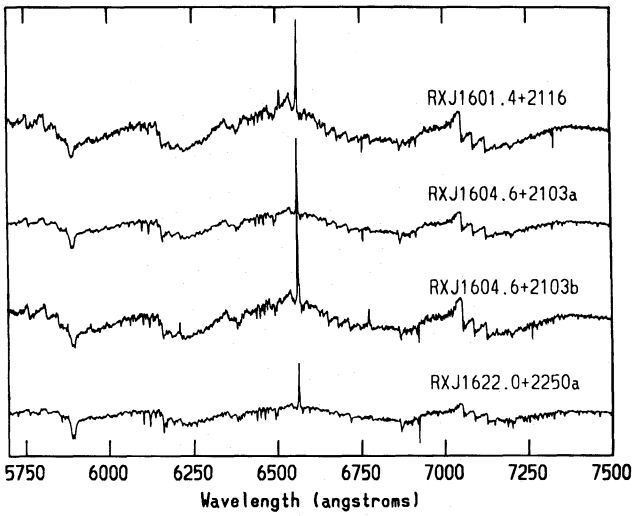

FIG. 8.—Broadband (5700–7500 Å) optical spectra for the dMe stars in our sample. The spectra have been normalized by a first-order cubic spline.

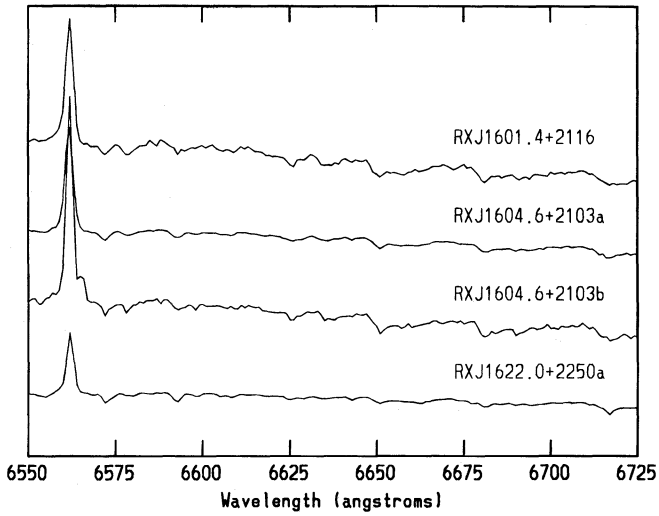

FIG. 9.—Same four stars as in Fig. 8, but with the region from 6550 Å to 6725 Å enlarged. The Hα line is readily noticeable, but there is no trace of the Li 6708 Å line in any of the spectra.

(1995b): in a region covering ~ 500 deg^2, 73 TTS were detected (Wichmann et al. 1995). As discussed at the end of § 2.2.2, if the region around MBM 40 were forming stars at the same rate as the Taurus molecular clouds, and given the areas surveyed and the relative distances, our technique would have uncovered two to three TTS in MBM 40.

4. DISCUSSION

From this exhaustive multiwavelength study of MBM 40, an example of a "compact" low-extinction cloud, we conclude that the cloud displays no evidence of recent or ongoing star formation. MBM 40 does not have the low-mass molecular cores typical of the Taurus-Auriga dark clouds, which are prolific nurseries of low-mass stars (see, e.g., Myers 1985). The clumps along the MBM 40 ridge are about the same size as the standard low-mass cores described by Myers, but the volume densities are likely to be smaller by at least 1 order of magnitude, and the line widths do not show evidence of subsonic turbulence. In addition, the column density and extinction throughout the cloud are lower by an order of magnitude from the values in dark clouds. In light of these differences, it may seem futile to search for young stars in the environs of MBM 40. However, the growing number of young stars discovered far from dark clouds or low-mass cores (§ 2) indicates that unconventional scenarios for forming low-mass stars must be explored.

MBM 40 is an atypical translucent cloud in that it appears to be gravitationally bound. Most translucent clouds have internal kinetic energies greater by a factor of 10–100 than the gravitational potential energy based on the cloud's mass and size. MBM 40 has nearly identical values of these two quantities and is most likely a bound object. This peculiar property of MBM 40 motivated our search for pre–main-sequence stars in this cloud.

Only five of 28 high-latitude clouds with the appropriate estimates of mass, radius, and velocity dispersions for the calculation of the ratio of kinetic to gravitational potential energy are gravitationally bound (Magnani, Hartmann, & Speck 1996a). One of these objects, MBM 20, *is* a star-forming region (Magnani et al. 1995). Using the data presented by Magnani et al. (1996a), we can compare the two objects: MBM 20 is slightly larger than MBM 40 (1.3 deg^2 vs. 0.7 deg^2) and has a larger mass (84 $M_\odot$ vs. 40 $M_\odot$); the internal velocity dispersion of the two objects is comparable (0.39 km s^{-1} vs. 0.25 km s^{-1}); and both objects have a compact morphology. The big difference between the two clouds is that MBM 20 contains a low-mass molecular core. The column density through the central region of MBM 20 is 3×10^{21} cm^{-2} (Liljeström 1991), a factor of 25 greater than the value for MBM 40 determined in § 2.2.1. Similarly, the extinction in the central region of MBM 20 is much larger than anywhere in MBM 40. Sandell et al. (1981) determine a lower limit to A_B of 5.6 mag over a $10' \times 5'$ area in the direction of the low-mass core. This opacity led Lynds (1962) to catalog MBM 20 as a dark cloud, although the outer regions are clearly translucent.

Another high-latitude translucent/dark cloud, MBM 12, has also formed T Tauri stars (Magnani et al. 1995; Pound 1996). Its physical characteristics are similar to those of MBM 20 with the exception that the ratio of kinetic to gravitational potential energy is ~ 26 (Magnani et al. 1996a). On the basis of our study, it appears that gravitational binding of the entire cloud is neither a necessary nor a sufficient condition for triggering the mechanism(s) responsible for producing stars in a translucent cloud and that a large column density of molecular gas in a low-mass core is a more important factor.

Comparative studies of the physical properties of the various types of translucent and dark clouds may illuminate under what conditions the star formation process begins in these objects. MBM 40, as an example of a compact, low-extinction, gravitationally bound cloud, is currently not capable of star formation. However, there are other types of translucent clouds that may be massive enough and that may harbor regions dense enough to have formed stars. These other types of clouds, specifically filamentary and compact, but of higher average extinction and thus greater $N(H_2)$ than MBM 40, are best exemplified by MBM clouds 55 and 7. Both of these objects have regions of greater extinction than those found in MBM 40 but lower than those in MBM 12 and MBM 20. In future papers, we will describe similarly exhaustive efforts to determine their role, if any, in local Galactic star formation.

This research has made use of the NASA/IPAC Extragalactic Database (NED) which is operated by the Jet Propulsion Laboratory, Caltech, under contract with the National Aeronautics and Space Administration. In addition, we have used the SIMBAD database, operated at CDS, Strasbourg, France. The *ROSAT* project has been supported by the Bundesministerium für Forschung und Technologie and the Max-Planck-Gesellschaft. Part of this research was supported by NASA grants NAG 5-2665 and NAG 5-1610 to the University of Georgia and NAGW-2698 to the Harvard-Smithsonian Center for Astrophysics. We thank an anonymous referee for comments which improved the presentation of this paper. We also thank Dave Burrows for providing us with the PSPC pointed observation of MBM 40 long before its public release.

REFERENCES

Alcalá, J. M., Krautter, J., Schmitt, J. H. M. M., Covino, E., Wichmann, R., & Mundt, R. 1995, A&A, 114, 109
Allamandola, L. J., & Tielens, A. G. G. M., ed. 1989, IAU Symp. 135, Interstellar Dust (Boston: Kluwer)
Allen, L. E., & Strom, K. M. 1995, AJ, 109, 1379
Blitz, L., Bazell, D., & Désert, F. X. 1990, ApJ, 352, L13
Blitz, L., Fich, M., & Stark, A. A. 1982, ApJS, 49, 183
Caillault, J.-P., Magnani, L., & Fryer, C. 1995, ApJ, 441, 261
Christodoulou, D. M., & Tohline, J. E. 1990, ApJ, 363, 197
Colomb, F. R., Pöppel, W. G. L., & Heiles, C. 1980, A&AS, 40, 47
Conlon, E. S. 1993, in ASP Conf. Ser. 45, Luminous High-Latitude Stars, ed. D. D. Sasselov (San Francisco: ASP), 33
Cruddace, R. G., Hasinger, G. R., & Schmitt, J. H. M. M. 1988, in Proc. ESO Conf. on Large Astronomical Databases, ed. F. Murtaugh (Garching: ESO), 177
Désert, F. X., Bazell, D., & Boulanger, F. 1988, ApJ, 334, 815
de la Reza, R., Torres, C. A. O., Quast, G., Castilho, B. V., & Veira, G. L. 1989, ApJ, 343, L61
de Vries, H. W. 1988, Ph.D. thesis, Columbia Univ.
Dickman, R. W. 1978, ApJS, 37, 407
Downes, R. A., & Keyes, C. D. 1988, AJ, 96, 777
Drdla, K., Knapp, G. R., & van Dishoeck, E. F. 1989, ApJ, 345, 815
Dwek, E. 1986, ApJ, 302, 363
Dyson, J. E., & Hartquist, T. W. 1983, MNRAS, 203, 1233
Elmegreen, B.G. 1993, in Protostars and Planets III, ed. E. H. Levy & J. I. Lunine (Tucson: Univ. of Arizona Press), 97
Evans, N. G., II, Zuckerman, B., Morris, M., & Sato, T. 1975, ApJ, 196, 433
Feigelson, E. D., Jackson, J. M., Mathieu, R. D., Myers, P. C., & Walter, F. M. 1987, AJ, 94, 1251
Fleming, T. A., Liebert, J., Gioia, I. M., & Maccacaro, T. 1988, ApJ, 331, 958
Gagné, M., & Caillault, J.-P. 1994, ApJ, 437, 361

Gir, B.-Y., Blitz, L., & Magnani, L. 1994, ApJ, 434, 162
Gliese, W., & Jahreiss, H. 1988, Ap&SS, 142, 49
Gredel, R., van Dishoeck, E. F., de Vries, C. P., & Black, J. H. 1992, A&A, 257, 245
Gregorio-Hetem, J., Lépine, J. R. D., Quast, G. R., Torres, C. A. O., & de la Reza, R. 1992, AJ, 103, 549
Guhathakurta, P., & Cutri, R. M. 1994, in ASP Conf. Ser. 58, The First Symposium on the Infrared Cirrus and Diffuse Interstellar Clouds, ed. R. M. Cutri & W. B. Latter (San Francisco: ASP), 34
Hasinger, G., Burg, R., Giacconi, R., Hartner, G., Schmidt, M., Trümper, J., & Zamorani, G. 1993, A&A, 275, 1
Heithausen, A., Mebold, U., & de Vries, H. W. 1987, A&A, 179, 263
Jura, M. 1979, ApJ, 227, 798
Keenan, F. P., Lennon, D. J., Brown, P. J. F., & Dufton, P. L. 1986, ApJ, 307, 694
Kenyon, S., & Hartmann, L. 1995, ApJS, 101, 117
Keto, E. R., & Myers, P. C. 1986, ApJ, 304, 466
Lance, C. M. 1988, ApJ, 334, 927
Lépine, J. R. & Duvert, G. 1994, A&A, 286, 60
Liljeström, T. 1991, A&A 244, 483
Lynds, B. T. 1962, ApJS, 7, 1
———. 1965, ApJS, 12, 1
Maccacaro, T., Gioia, I. M., Wolter, A., Zamorani, G., & Stocke, J. T. 1988, 326, 680
Magnani, L. 1994, in ASP Conf. Ser. 58, The First Symposium on the Infrared Cirrus and Diffuse Interstellar Clouds, ed. R. M. Cutri & W. B. Latter (San Francisco: ASP), 160
Magnani, L., Blitz, L., & Mundy, L. 1985, ApJ, 295, 402 (MBM)
Magnani, L., Blitz, L., & Wouterloot, J. G. A. 1988, ApJ, 326, 909
Magnani, L., Caillault, J.-P., & Armus, L. 1990, ApJ, 357, 602
Magnani, L., Caillault, J.-P., Buchalter, A., & Beichman, C. A. 1995, ApJS, 96, 159
Magnani, L., Hartmann, D., & Speck, B.G. 1996, ApJS, submitted
Magnani, L., & Onello, J. S. 1995, ApJ, 443, 169
Magnani, L., Onello, J. S., Hartmann, D., & Thaddeus, P. 1996, in preparation
Mathis, J. S., Rumpl, W., & Nordsieck, K. H. 1977, ApJ, 217, 425
Mebold, U., Heithausen, A., & Reif, K. 1987, A&A, 180, 213
Meyerdierks, H., Brouillet, N., & Mebold, U. 1990, A&A, 230, 172
Morrison, R. & McCammon, D. 1983, ApJ, 270, 119
Myers, P. C. 1985, in Protostars and Planets II, ed. D. C. Black & M. S. Matthews (Tucson: Univ. of Arizona Press), 81
Myers, P. C., & Benson, P. J. 1983, ApJ, 266, 309
Neuhäuser, R., Sterzik, M. F., Schmitt, J. H. M. M., Wichmann, R., & Krautter, J. 1995a, A&A, 297, 391
———. 1995b, A&A, 295, L5
Neuhäuser, R., Sterzik, M. F., Torres, G., & Martin, E. L. 1995c, A&A, 299, L13
Penprase, B. E. 1993, ApJS, 88, 433
Pfeffermann, E., et al. 1986, Proc. SPIE, 733, 519
Pound, M. W. 1996, ApJ, in press
Raymond, J. C., & Smith, B. W. 1977, ApJS, 35, 419
Reach, W. T., Pound, M. W., Wilner, D. J., & Lee, Y. 1995, ApJ, 441, 244
Rodgers, A. W., Harding, P., & Sadler, E. 1981, ApJ, 244, 912
Rucinski, S. M., & Krautter, J. 1983, A&A, 121, 217
Sandage, A. 1976, AJ, 81, 954
Sandell, G., Johansson, L. E. B., Nguyen-Q-Rieu, & Mattila, K. 1981, A&A, 97, 317
Schreieber, W., Wouterloot, J. G. A., Heithausen, A., & Winnewisser, G. 1993, A&A, 276, L5
Sharpless, S. 1959, ApJS, 4, 257
Snell, R. L., Mundy, L. G., Goldsmith, P. F., Evans, N.J., II, & Erickson, N. R. 1984, ApJ, 276, 625
Stocke, J. T., Morris, S. L., Gioia, I. M., Maccacaro, T., Schild, R., Wolter, A., Fleming, T. A., & Henry, J. P. 1991, ApJS, 76, 813
Sterzik, M. F., Alcalá, J. M., Neuhäuser, R., & Schmitt, J. H. M. M. 1995, A&A, 297, 418
Townes, C., & Cheung, A. C. 1969, ApJ, 157, L103
Trümper, J. 1983, Adv. Space Res., 2, 241
Turner, B. E. 1993, ApJ, 410, 140
Turner, B. E., Xu, L., & Rickard, L. J. 1992, ApJ, 391, 158
Ungerechts, H., & Thaddeus, P. 1987, ApJS, 63, 645
van Dishoeck, E. F., & Black, J. H. 1988, ApJ, 334, 771
Verschuur, G. L. 1974, ApJS, 27, 283
Verter, F., Magnani, L, Dwek, E., & Rickard, L. J. 1996, in preparation
Verter, F., & Rickard, L. J. 1996, in preparation
Walter, F. M., Brown, A., Mathieu, R. D., Myers, P. C., & Vrba, F. J. 1988, AJ, 96, 297
Weiland, J. L., Blitz, L., Dwek, E., Hauser, M. G., Magnani, L., & Rickard, L. J. 1986, ApJ, 306, L101
Welty, D. E., Hobbs, L. M., Blitz, L., & Penprase, D. E. 1989, ApJ, 346, 232
Wichmann, R., et al. 1996, in preparation
Yun, J. L., & Clemens, D. P. 1990, ApJ, 365, L73
Zimmermann, H. U., Belloni, T., Izzo, C., Kahabka, P., & Schwentker, O. 1993, EXSAS User's Guide, MPE Report 244